Concept for a New Cloud Condensation Nucleus (CCN) Spectrometer

Timothy M. VanReken[1], Athanasios Nenes[2],

Richard C. Flagan[1], and John H. Seinfeld[1]

[1]Department of Chemical Engineering, California Institute of Technology

[2]Schools of Earth and Atmospheric Sciences and Chemical Engineering,

Georgia Institute of Technology

ABSTRACT

The design of a new cloud condensation nucleus (CCN) spectrometer based on modifications to the original design of Fukuta and Saxena (1979a) is presented. The key modifications include introducing a trapezoidal geometry and orienting the chamber vertically. A series of simulations demonstrate the broadening of the effective range of the instrument to include supersaturations lower than those reported for the original instrument, without reducing the maximum resolvable supersaturation. A design criterion is developed to eliminate configurations that would result in secondary flows in the growth chamber resulting from buoyancy effects. Using instrument configurations that satisfy this criterion, the effects of variations in the chamber geometry, the imposed temperature gradient, and the total volumetric flow are evaluated. A new configuration is identified that could produce real-time CCN spectra with an effective range including at least supersaturations between 0.07% and 1.2%.

INTRODUCTION

In order to improve our understanding of the role of aerosols in cloud development and propagation, it is necessary to measure the cloud-forming ability of the aerosol population under a wide variety of conditions. Those particles that have the potential to form cloud droplets at water vapor supersaturations in the range of those typically encountered in clouds are denoted cloud condensation nuclei, or CCN. CCN are characterized by their critical supersaturation (S_c), the supersaturation at which the particles can activate and form cloud droplets. Supersaturation, S, is defined as the amount by which the ratio of the water vapor pressure to the saturated vapor pressure at the same temperature exceeds unity. The critical supersaturation of a particle depends on its size and composition, and the cloud-forming potential of the aerosol population can be characterized by expressing the CCN number concentration as a function of supersaturation.

In practice, CCN concentrations are typically measured by exposing an aerosol sample to a known supersaturation profile for a period sufficient for growth to droplet size, at which point the grown droplets can be readily detected using standard light scattering techniques. The supersaturation required to activate droplets is most commonly induced in an instrument by maintaining two parallel wet surfaces at different temperatures. The linear temperature and water vapor concentration profiles between the two surfaces lead to a supersaturation in water vapor between them, since the saturation water vapor pressure is a sublinear function of temperature. Larger temperature differences lead to larger supersaturations, and the maximum supersaturation is located

approximately midway between the two surfaces. Several distinct designs employ this same basic concept (e.g., Twomey, 1963; Sinnarwalla and Alofs, 1973); others employ a cylindrical geometry and take advantage of the different diffusion rates of heat and water vapor (Chuang et al., 2000a; Roberts and Nenes, 2003). Regardless of design, all aforementioned instruments are characterized by an important limitation: they can only measure one supersaturation at a time. To produce CCN spectra with a time resolution sufficient for airborne measurements, an instrument should employ continuous flow, and should be able to make measurements at multiple supersaturations simultaneously. While single supersaturation CCN counters are frequently used for field measurements (e.g., Chuang et al., 2000b; Snider and Brenguier, 2000; VanReken et al., 2003) and can provide valuable information regarding the activation properties of the aerosol population, they do not unambiguously characterize the CCN spectrum on a timescale appropriate for airborne measurements.

There are instruments capable of measuring the activation properties of an aerosol sample simultaneously over a broad range of supersaturations. One such instrument, developed by Hudson (1989), exposes the aerosol sample to a supersaturation that increases in the direction of flow. CCN with different critical supersaturations activate at different points along their streamline, and thus have different growth times; the CCN spectrum is inferred from the droplet size distribution at the outlet. The relationship between particle critical supersaturation and outlet diameter is derived from calibrations using particles of known size and composition. The assumption that particles with the same critical supersaturation will always grow at the same rate is fundamental to the

measurement, but recent studies indicate that this assumption does not always hold for all particle compositions. There is evidence that organic compounds can affect both the equilibrium droplet diameter (Shulman et al., 1996; Facchini et al., 1999) and the rate at which the droplets grow to their equilibrium size (Feingold and Chuang, 2002; Chuang, 2003). When there is a significant organic component to the atmospheric aerosol, reliable CCN data would be quite valuable, since the importance of organic species in cloud processes is largely uncertain. In such a situation, an inferred CCN spectrum based on calibration with a salt aerosol may lead to an inaccurate result.

Fukuta and Saxena (1979a, 1979b) developed an instrument that is able to measure the activation properties of an aerosol population without relying on the final size of the resultant droplet. Instead of exposing the entire sample to an identical saturation profile, this instrument, denoted hereafter as the Fukuta-Saxena CCN Spectrometer (FSCS), imposes a transverse saturation gradient in the growth chamber, so that different streamlines are exposed to different supersaturation profiles. The principle is described in detail by Fukuta and Saxena (1979b). Additional insight was provided by later simulations of the instrument (Nenes et al., 2001a). In the FSCS, both the top and bottom plates of the growth chamber have an imposed temperature gradient perpendicular to the direction of flow, so that the temperature difference between the plates (and, therefore, the supersaturation) is greater at one side of the rectangular chamber than at the other. The gradient is maintained by controlling the temperature of both the top and bottom plates at one end of the growth chamber (Figure 1a); the side wall at the temperature controlled end is made of a material with low thermal conductivity, while the opposite

side wall and both plates are constructed of a highly conductive material. Heat therefore flows from the high temperature edge through the conductive material to the low temperature edge. The activated droplets exiting the growth chamber on different streamlines are counted separately, so that the supersaturation at which a droplet activated is determined by its position on the transverse axis and not by its outlet size.

The utility of the FSCS is somewhat limited by a relatively small dynamic range. Fukuta and Saxena (1979a) gave the range as $0.15 < S < 1.2\%$; data presented in later studies (DeFelice and Saxena, 1994; Saxena, 1996) all fall within those limits. DeFelice and Saxena (1994) stated that higher or lower supersaturations could be attained by adjusting the temperatures of the saturated plates; a reduction in the lower bound would be a significant improvement, since clouds with maximum supersaturations less than 0.1% are thought to be common and climatically important (Pruppacher and Klett, 1996).

Nenes et al. (2001a) developed a model to simulate the FSCS and determine the theoretical limitations to its dynamic range. They concluded that the instrument could not resolve the CCN spectrum when $S < \sim 0.1\%$, due to insufficient growth times. Increasing the growth time (either by lengthening the growth region or reducing the flow rate) did not improve performance, since growing droplets will tend to gravitationally settle out of the region of maximum supersaturation, further reducing the growth rate and causing particle losses. A vertical orientation for the growth chamber (where the flow is in the direction of gravity) was simulated as an alternative and found to be generally more effective, as it eliminated the problem of gravitational settling. However, operating

the FSCS vertically introduces a new complication, that of buoyancy-induced secondary flows; Saxena and Carstens (1971) have previously noted the potential impact of buoyancy flows on CCN measurements. If the imposed temperature difference between the two plates is too large, the variations in air density cause flow reversals along some streamlines. In the end, Nenes et al. (2001a) concluded that orienting the growth chamber vertically would match, but not significantly improve upon, the empirically demonstrated performance of the instrument.

The analysis of the FSCS design presented by Nenes et al. (2001a) suggests potential mechanisms by which the minimum resolvable supersaturation might be reduced. For particles of low critical supersaturation, the rate of droplet growth is effectively proportional to the supersaturation (Seinfeld and Pandis, 1998), so much more time is required to separate activated droplets from other particles at low supersaturations. The minimum resolvable supersaturation could be decreased by increasing the residence time for those streamlines, either by reducing the flow velocity or by lengthening the column. However, in a vertically-oriented chamber, the flow velocities along the high supersaturation streamlines must be large enough that buoyancy-induced flow reversals do not significantly impact the flow of the aerosol sample through the growth chamber. The dynamic range of the FSCS could be significantly increased if the flow velocity for the low supersaturation streamlines could be reduced without reducing the velocity significantly on the high supersaturation streamlines.

The current work details a means of doing this through the conceptual design of a new CCN spectrometer. By redesigning the geometry of the FSCS growth chamber, a transverse gradient in the flow velocities of streamlines can be achieved, so that streamlines exposed to low supersaturations have significantly longer residence times than more highly supersaturated streamlines. A trapezoidal geometry is chosen here (Figure 1b), but other more complex geometries can have similar effects, potentially with even more dynamic range. The design of the growth chamber depends largely on three parameters: the shape of the chamber, the imposed temperature gradient, and the volumetric flow rate through the instrument. The simulations in this work use a model similar to that used by Nenes et al. (2001a) to examine how varying these parameters affects supersaturation profiles and particle growth in the instrument. The modifications to the model necessary to simulate the proposed geometry are discussed, and the potential impact of buoyancy forces is evaluated. By optimizing the primary design parameters, a growth chamber can be designed to resolve droplets at supersaturations significantly lower than is possible using the FSCS, with little variation in performance based on the composition of the sample aerosol. A CCN spectrometer based on this design would be able to produce activation data over the range of supersaturations of climatic interest rapidly enough for airborne measurements, without being sensitive to the variations in droplet growth rate introduced by variations in chemical composition.

INSTRUMENT MODEL

To evaluate the performance of several existing CCN instrument designs (including the FSCS), Nenes et al. (2001a) developed a model that determines the theoretical

temperature, water vapor, and supersaturation distributions as a function of position. These distributions were then used to calculate particle growth and. activation In the case of the FSCS, the authors chose to treat the growth chamber as a series of two-dimensional flow fields where each streamline is treated as flow between two infinite plates; any perturbations to the velocity field arising from the proximity of the side walls is neglected. This approach is based on scaling arguments and is consistent with experimental data reported by Fukuta and Saxena (1979a); the simulations are valid if the distance from the chamber side walls for the chosen streamlines for the simulations is not significantly less than the distance between the hot and cold plates. This work uses the numerical model developed by Nenes et al. (2001a) to examine the effects of replacing the rectangular shape of the FSCS with a trapezoidal geometry (Figure 1b). The specifics of the model formulation are discussed at length in the earlier work, and will not be repeated here.

Some modifications to the model developed by Nenes et al. (2001a) are required to accommodate a trapezoidal geometry. In the original formulation used to simulate the FSCS, the temperature of the hot and cold plates varied based on the chosen value of the z coordinate (Figure 1a), but the distance between the plates and the initial velocity profile did not. For a trapezoidal geometry (Figure 1b), both the distance between plates and the velocity (u) profile at the inlet become a function of the z position. The distance between the plates is a linear function of z:

$$H(z) = H_{\max} - \frac{(H_{\max} - H_{\min})}{W} z \,. \qquad [1]$$

The inlet velocity distribution is:

$$u(y,z) = \frac{6Q}{W(H^*)^3}(H(z))^2\left[1-\left(\frac{2y}{H(z)}\right)^2\right], \qquad [2]$$

where Q is the volumetric flow through the chamber and

$$(H^*)^3 = \mathrm{H}_{\max}^3 + H_{\max}^2 H_{\min} + H_{\max} H_{\min}^2 + H_{\min}^3 . \qquad [3]$$

The analysis leading to the result in equation [2] are available in VanReken (2004), as are equations describing dependence on z of the temperatures of the hot and cold plates.

EFFECT OF BUOYANCY FORCES

When a chamber with a temperature difference between two plates is oriented vertically, so that the flow moves downward in the direction of the gravitational force, there exists a buoyancy force that acts to perturb the expected laminar parabolic flow profile. The perturbation is strongest where the temperature difference between opposite plates is greatest (i.e., for low values of z), and can be large enough for the flow to reverse direction near the warm plate. Such a reversal in fact occurs when the chamber design of the original FSCS is oriented vertically (Figure 2). The velocity profiles shown are at a point midway down the length of the growth chamber, after the equilibrium velocity field is established. The occurrence of flow reversal within the growth chamber might not appear significant when examining simulation results, but as a practical matter would complicate instrument design; recirculation of activated droplets would be likely, and flow oscillations or significant flow across the width of the chamber might also occur.

It is important to establish the conditions under which a proposed growth chamber design is not susceptible to flow reversals. An earlier analysis by Saxena and Carstens (1971) estimated the magnitude of the buoyancy flow between vertical parallel plates held at different temperatures. Their work can be improved upon by deriving a design criterion to determine whether for a set of design parameters the possibility exists for a negative value of u at any location in the chamber. Following Bird et al. (1960), and employing the Boussinesq approximation, the velocity field at a given value of z between infinite vertical plates of temperature difference ΔT is

$$u(\eta, z) = \frac{g\rho\Delta T}{48T\mu}(H(z))^2\left[\eta^3 - A\eta^2 - \eta + A\right], \qquad [4]$$

where $\eta = (2y/H(z))$ and A is an undetermined constant. For the purpose of deriving a design criterion, the gravitational force, g, the density, ρ, and the viscosity, μ, can be treated as constant. The terms on the right side of the equation outside the brackets can be grouped and denoted Γ. To determine the value of A, we integrate the velocity over all values of η:

$$u_{avg}(z) = \int_{-1}^{1} u(\eta, z)d\eta, \qquad [5]$$

which results in

$$A = \frac{3u_{avg}(z)}{4\Gamma}. \qquad [6]$$

Substituting this result into equation [4] and rearranging terms:

$$u(\eta, z) = \left[\frac{3}{4}u_{avg}(z) - \Gamma\eta\right](1 - \eta^2) \quad . \qquad [7]$$

Since the range of possible values for η is between -1 and 1 (inclusive), for the velocity to be less than zero (indicating flow reversal), the first bracketed term on the right side of the equation must be less than zero. Therefore, flow reversal will not occur if

$$\frac{4\Gamma}{3u_{avg}(z)} < 1. \qquad [8]$$

Equation [8] assumes that $\eta = 1$; this gives the largest possible value to the numerator, making the design criterion as conservative as possible. Substituting for Γ and $u_{avg}(z)$ (which is two-thirds of $u_{max}(z)$ from equation [2]) yields the buoyancy criterion, B, in a form more convenient for design purposes:

$$B = \frac{1}{144}\frac{g\rho}{\mu}\frac{(\Delta T)}{T}\frac{WH^*}{Q} < 1. \qquad [9]$$

Equation [9] is the desired design criterion that should be satisfied to ensure that flow reversal would not occur in a proposed instrument configuration. Calculating B for the original FSCS configuration confirms that flow reversal would be expected (Table 1). Likewise, if a set of instrument parameters is selected so that the design criterion is satisfied (the "Baseline Configuration" in Table 1), then flow reversal does not occur (Figure 2). There exist some configurations where $B > 1$ that still would not result in a flow reversal, but this study will only consider configurations where the criterion is satisfied.

INSTRUMENT DESIGN SIMULATIONS

The primary motivation for exploring alternative designs for a transverse gradient CCN spectrometer is the need for accurate measurements at supersaturations below 0.1%.

Several instrument parameters affect the resolvable supersaturation range; this study will explore the sensitivity of the lower end of the range to changes in the geometry of the growth chamber, the imposed temperature gradient, and the flow rate through the chamber. To provide a reasonable baseline against which to compare the effects of parameter variations, the performance of the original FSCS design and a smaller chamber with the same geometry are also simulated using the reformulated instrument model.

Baseline Simulations

Nenes et al. (2001a) included instrument simulations of the FSCS in their study of the theoretical properties of various CCN instrument designs, but the volumetric flow rate considered results in higher velocities than reported by Fukuta and Saxena (1979a). To verify the predictive ability of the new model, the original FSCS is again simulated in this study, even though the configuration does not satisfy the design criterion and leads to a reversed flow near the warm plate (Figure 2). Also simulated is a theoretical instrument with the same (rectangular) geometry as the FSCS, but with approximately a 60% reduction in width, a 50% decrease in the plate separation, and a 70% reduction in the volumetric flow rate. Reducing the width of the chamber would make the instrument significantly lighter (an important factor in the design of airborne instrumentation), with little change in instrument performance; the values for H and Q were chosen such that the baseline configuration would be similar in performance to the original FSCS while satisfying the buoyancy criterion. The instrument parameters and operating conditions for these simulations are detailed in Table 1.

The new baseline configuration results in a reduction in the maximum resolvable supersaturation, but the minimum resolvable supersaturation is not significantly different in the two cases. Supersaturation profiles for the original FSCS design (Figure 3a) and for this study's baseline design (Figure 4a) show how the equilibrium supersaturation profile depends on the cross-gradient position within the growth chamber. In both figures, each curve represents the centerline supersaturation for a different value of *z*. Each curve increases to its equilibrium supersaturation from a minimum (not shown in the figures) near the point where the imposed wetted surfaces at the warm and cold plates begin. As expected, the largest supersaturations occur at the lowest values of *z*, where the difference in temperature between the hot and cold plates is largest; the maximum supersaturation is approximately 1% for the original FSCS configuration, and 0.8% for the baseline. The saturation profiles also indicate what fraction of the total length of the growth chamber is available for particle growth. In each of these cases, the profiles for low values of *z* approach their equilibrium values sooner than those profiles at the lower-supersaturation end of the chamber. This result limits the time available for droplet growth for those streamlines where *S* is lower.

The effect of the limited growth times at low supersaturations can be seen in the particle growth curves (Figures 3b and 4b for the original FSCS and baseline designs, respectively). The curves display the outlet droplet diameter as a function of the critical supersaturation of the dry particles entering the instrument. As before, each curve represents the performance on the centerline for the given value of *z*. The critical supersaturation of a particle is a function of its size and composition (as described by

Köhler theory; Seinfeld and Pandis, 1998); these simulations assume a pure ammonium sulfate composition, and that the water accommodation coefficient (α) is 1.0. The solid black line in each figure represents the critical diameter, which is the size of the droplet when it has reached its critical supersaturation. If the outlet diameter at a given supersaturation is greater than the critical diameter at that point, then those particles have activated. The "sharpness" of the elbow in the individual growth curves is an indication of effectiveness of the instrument in separating the activated droplets from the rest of the sample.

For the original FSCS design (Figure 3b) and this study's baseline configuration (Figure 4b), those streamlines with equilibrium supersaturations greater than about 0.2% indicate a sharp size differentiation between the particles that activate and those that do not. As the value of z increases and the equilibrium supersaturation decreases, the difference in outlet diameter between activated and unactivated particles diminishes. When the z-value is such that the particles are exposed to a supersaturation of about 0.1% or less (i.e., $z > 0.125$ m for the original design and $z > 0.045$ m for the baseline case), the elbow in the growth curve is not sufficiently distinct to reliably separate the activated particles from unactivated ones; this sets a lower limit on the instrument's resolution. Thus the simulation results indicate for original FSCS configuration, the resolvable supersaturation range is from ~0.1 - 1%, in general agreement with the performance of the actual instrument (Fukuta and Saxena, 1979a). In the baseline configuration, the upper end of the resolvable range is somewhat reduced, to ~0.8%.

Variations in Growth Chamber Geometry

As noted earlier, the lower limit to the resolvable supersaturation range is a result of there being insufficient time for the particles on streamlines with low supersaturations to grow to droplet size; the residence time for growth along these streamlines could be increased by implementing a trapezoidal geometry. A series of simulations, where the difference in plate spacing on opposite ends of the growth chamber ($\Delta H = H_{max} - H_{min}$) is gradually increased, show how an alternative geometry can improve the resolvable range. For these simulations, H_{min} is reduced by the same amount that H_{max} is increased from the baseline height (e.g., when ΔH is 0.008 m, H_{max} is set to 0.013 m and H_{min} to 0.005 m); this ensures that the cross-sectional area of the growth chamber remains unchanged.

The centerline velocity variations for these simulations are presented in Figure 5. Taken at a point after the flow field is well-established, the data clearly show the effect of the trapezoidal geometry on the velocity profiles. The rectangular geometry (where ΔH is zero) produces no velocity gradient across the width of the chamber; the centerline velocity for this geometry is near 0.060 m s^{-1} for all values of z where wall effects can be ignored. As ΔH is increased, and the geometry becomes "more" trapezoidal, the gradient in the centerline velocity across the width of the chamber becomes greater. When the height difference is 0.010 m, the largest considered in this study, the velocity at the low supersaturation end of the column is less than 20% of the velocity at the opposite end (0.017 m s^{-1} versus 0.089 m s^{-1}). This gives the particles exposed to lower supersaturations the longer residence time required for droplet growth. Compared to the

baseline configuration, there is a fourfold increase in the time available for droplet growth when ΔH = 0.010 m for the streamlines exposed to lowest supersaturations.

The effects of modifying the chamber geometry can be seen in the growth curves in Figure 6. The data from two transverse locations are shown: one at the high supersaturation end of the chamber (z = 0.010 m), and one from the low supersaturation end (z = 0.050 m). On the low supersaturation end, increasing the value of ΔH to 0.010 m (the maximum value considered here) results in an approximate doubling of the outlet droplet diameter. At z = 0.050 m, this doubling increases the size difference between activated and unactivated particles, thereby reducing the minimum resolvable supersaturation to approximately 0.08%. This improvement at the low end of the supersaturation range is achieved without any corresponding reduction in the maximum resolvable supersaturation. At the high supersaturation end of the chamber, the activated droplets are smaller at the outlet; this is not an issue, since the droplets are still larger than those exposed to lower supersaturations.

Another potential limitation should be noted, even though it does not occur for any of the cases examined here. When the saturation profiles arising from the trapezoidal geometry (Figure 7) are compared with the baseline case (Figure 3a), the effect of the increased residence times at the low supersaturation end of the chamber is obvious- at high values of z, streamlines reach their equilibrium state much more quickly when ΔH = 0.010 m than in the baseline case. However, the opposite effect is seen where the equilibrium supersaturation is not reached until the streamlines have proceeded more than

halfway down the length of the chamber, due to the higher flow velocities. In an extreme case, the streamlines at the high supersaturation end of the chamber might never reach their equilibrium supersaturations; this would result in a reduction in the maximum resolvable supersaturation in the chamber, an undesirable outcome.

Variations in Temperature Gradient

As has been noted by Fukuta and Saxena (1979a) and DeFelice and Saxena (1994), the range of supersaturations in the growth chamber can be moved by changing the temperature difference (ΔT) between the hot and cold edges (T_{H0} and T_{C0} in Figure 1). The response of a chamber with the proposed trapezoidal geometry to changes in ΔT is explored here by increasing or decreasing T_{H0} without changing T_{C0} (*i.e.*, when ΔT = 3.5 K, T_{H0} = 286.5 K and T_{C0} = 283 K). A value of 0.006 m was chosen for ΔH for these simulations. This maximizes the range over which the temperature can be varied while still ensuring that B is less than unity and retaining the resolution enhancements achieved with the trapezoidal geometry. The effects of the temperature variations on particle growth are as expected (Figure 8); as ΔT is increased, the upper boundary of the supersaturation range increases. The effective supersaturations of streamlines at the opposite end of the chamber (i.e., where the distance between plates is smaller) also increase, but this undesirable effect is mitigated because the increase in ΔT also allows activation to occur on streamlines where it had not for lower values of ΔT. For example, when ΔT is increased from 5.0 K (the value for the simulations where the geometry was varied) to 6.5 K, the effective supersaturation increases from ~0.8% to ~1.3% at z = 0.010 m, and from ~0.08% to ~0.2% at z = 0.050 m. However, the increased temperature

gradient now allows particles to activate on the z = 0.055 m streamline, where there was no activation before; the effective supersaturation at that position is ~0.07%. Thus by increasing ΔT it is possible to improve both the upper and lower boundaries of the resolvable supersaturation range.

Volumetric Flow Rate Variation

The total volumetric flow rate (Q) through the trapezoidal chamber is also varied to demonstrate its effect on particle growth. From the baseline value of 2.50 x 10^{-5} m^3 s^{-1}, Q is increased by 10% and decreased by 15%, in increments of 5%. To ensure that the buoyancy criterion is satisfied for these simulations, a value of 5.5 K is chosen for ΔT. The results (Figure 9) show that lower flow rates lead to somewhat larger outlet diameters, with a negligible effect on the supersaturation range. The highest simulated flow rate, 2.75 x 10^{-5} m^3 s^{-1}, is 30% larger than the lowest value. At z = 0.010 m, this variation results in an increase in the outlet droplet diameter of approximately 30%; at the low supersaturation end of the chamber (i.e., where z = 0.050 m), the improvement is even less, about 15%. Additional reductions to the flow rate could further increase the outlet diameters, but such a configuration would not satisfy the buoyancy criterion. Since the droplets are large enough in all cases examined here to be detected by light scattering, there is little advantage in reducing the volumetric flow rate to increase the outlet diameter.

RESPONSE TO AEROSOL NON-IDEALITIES

The simulations presented in the previous section demonstrate the relative effects of changes in the chamber geometry, the temperature gradient, and the total volumetric flow. The results indicate that larger values of ΔH and ΔT can improve the resolvable supersaturation range of the instrument, but that varying Q has a minimal effect. Although there is no single optimum configuration, it is possible to choose a configuration that results in both a large resolvable supersaturation range and a sharp size differential between activated and unactivated particles while still satisfying the buoyancy criterion to avoid flow reversal.

The simulation results for one such configuration are presented in Figure 10. For this design, ΔH is set to 0.010 m and ΔT is 6.0 K. To keep the buoyancy criterion below 1.0, the volumetric flow rate is 2.75×10^{-5} m^3 s^{-1}. All other parameters are as in the baseline configuration, and the results are still based on an idealized aerosol (i.e., pure ammonium sulfate aerosol with α set equal to 1.0). The saturation curves in Figure 10a indicate that the maximum equilibrium supersaturation is approximately 1.2%, roughly the same as that of the original FSCS. The growth curves confirm this maximum supersaturation, and show that particles with critical supersaturations as low as 0.07% would be easily resolved by the instrument. In fact, the sharp size difference between activated and unactivated droplets at z = 0.055 m in Figure 10b implies that particle activation would likely occur on streamlines between z = 0.055 m and z = 0.060 m. This would probably extend the resolvable supersaturation range below S = 0.07%.

The aerosol growth calculations to this point have been based on an idealized aerosol (pure ammonium sulfate, α = 1.0). As was noted in the introduction, a primary advantage of the FSCS (as well as the alternative configuration proposed here) over other designs is its relative insensitivity to variations in droplet size resulting from non-homogeneous aerosol populations. To verify the performance of the proposed configuration, an alternative aerosol growth model was employed that allows more realistic aerosol populations to be simulated. The sensitivity of the proposed instrument configuration to variations in chemical composition was tested by comparing the growth calculations for a pure salt aerosol to a population that is 50% insoluble (internally mixed, by mass) and to one that is 90% insoluble. The results are presented in Figure 11a; note that this growth model results in smaller droplets at the outlet for specified inlet composition due to a change in the method for calculating the wet diameter at the inlet. For the two streamlines presented in Figure 11a, the results indicate that varying the composition has a minimal effect of the effective supersaturation of the streamline. The effect on the outlet diameter is also relatively small at the high supersaturation end of the chamber (i.e., when z = 0.010 m), but at low supersaturations there is a significant reduction in outlet size when the aerosol is primarily composed of insoluble material. However, this does not directly affect the resolution of the instrument; since the "sharpness" of the elbow is not diminished, activated droplets can still be readily distinguished from unactivated particles. It is possible that the apparent reduction in growth rate for slightly soluble particles could cause the minimum resolvable supersaturation to shift slightly toward a larger value.

The effect of the value of the water mass accommodation coefficient on the growth calculation can be seen by comparing Figure 11b with Figure 10b. Studies have indicated that for a growing water droplet, α may have values as low as 0.04 (Chodes et al., 1974; Shaw and Lamb, 1999); the growth curves in Figure 11b were calculated with α set to 0.04. The growth curve for $\alpha = 1.0$ at the highest supersaturation streamline (z = 0.010 m) is included for comparison. When the lower value of the accommodation coefficient is used in the calculation, there is a significant (~50%) reduction in the outlet diameter of the activated droplets. While there are still sharp gradients in the growth curves on those streamlines with high effective supersaturations, it is no longer possible to distinguish between the activated droplets and the unactivated particles on streamlines where the effective supersaturation is less than ~0.2%. If the value of α was even less than 0.04, the performance of the proposed instrument (as well as designs currently in use) would break down completely. If the mass accommodation coefficient is significantly greater than 0.04, as has been suggested recently by Li et al. (2001), then the performance of the proposed configuration would be closer to the idealized case discussed above.

The results presented here demonstrate that it is possible to design a CCN spectrometer with a broader range than the FSCS. The performance of such an instrument would have a minimal dependence on compositional variability in the sample aerosol, unless the mass accommodation coefficient was affected by those changes; the latter could result in undercounting at supersaturations at the low end of the instrument's resolvable range, but not over the entire range. In that sense, all CCN instruments are

susceptible to changes in α. Obviously, alternative configurations to the one described here could have similar characteristics, or different characteristics better suited for a given design goal. Other practical details of the instrument design would also interplay with the parameters considered here, and would influence choices for the chamber design; such considerations are beyond the scope of this work.

SUMMARY AND CONCLUSIONS

This work explores the viability of alternative growth chamber geometries to that used in the original Fukuta-Saxena CCN Spectrometer. By introducing a trapezoidal cross section, the flow within the growth chamber is redistributed to allow longer growth times for those particles exposed to lower supersaturations while minimizing the potential impact of buoyancy forces. A design criterion is derived that determines whether a given design configuration is susceptible to flow reversal under equilibrium conditions. Using only configurations that satisfy this buoyancy criterion, a series of simulations are presented that demonstrate the relative effects of varying the chamber shape, the temperature gradient, and the total flow rate through the instrument.

Simulation results indicate that the incorporation of a trapezoidal geometry significantly increases the growth time available for particles on streamlines at the low supersaturation end of the growth chamber. This allows activated particles on these streamlines to reach a size where they can be easily differentiated from unactivated particles, thereby reducing the minimum resolvable supersaturation of the instrument, without sacrificing resolution at the upper end of the range. Increasing the temperature

gradient in a given configuration generally results in an upward shift of the entire resolvable supersaturation range. However, the results here indicate that in some cases increasing ΔT will also result in activation on streamlines where it would not otherwise occur; thus, it is possible to increase the upper limit of the resolvable range without sacrificing resolution at lower supersaturations. Compared with the effects of varying the shape of the chamber and the temperature gradient, modest variations in the total volumetric flow are found to have a relatively small impact on instrument performance.

By using the buoyancy criterion developed in this work and applying the results of the growth chamber simulations, it is possible to design a CCN spectrometer with a broader dynamic supersaturation range that would be better suited for real-time atmospheric CCN measurements than currently available instruments. One such configuration is presented here, which would result in a dynamic range of $0.07\% < S < 1.2\%$. This compares favorably with the FSCS, which has the same maximum resolvable supersaturation, but has not been shown to able to resolve supersaturations below ~0.1%.

Acknowledgements. This work was supported by the Office of Naval Research and the EPA STAR Graduate Fellowship Program.

REFERENCES

Bird, R. B., Stewart, W. E., and Lightfoot, E. N. (1960). *Transport Phenomena.* John Wiley & Sons, New York.

Chodes, N., Warner, J., and Gagin, A. (1974). A Determination of the Condensation Coefficient of Water from the Growth Rate of Small Cloud Droplets, *J. Atmos. Sci.*, 31:1351-1357.

Chuang, P. Y., Nenes, A., Smith, J. N., Flagan, R. C., and Seinfeld, J. H. (2000a). Design of a CCN Instrument for Airborne Measurement, *J. Atmos. Oceanic Technol.*, 17:1005-1019.

Chuang, P. Y., Collins, D. R., Pawlowska, H., Snider, J. R., Jonsson, H. H., Brenguier, J.-L., Flagan, R. C., and Seinfeld, J. H. (2000b). CCN Measurements during ACE-2 and Their Relationship to Cloud Microphysical Properties, *Tellus Ser. B,* 52:843-867.

Chuang, P. Y. (2003). Measurement of the Timescale of Hygroscopic Growth for Atmospheric Aerosols, *J. Geophys. Res.*, 4282, doi:10.1029/2002JD002757.

DeFelice, T. P. and Saxena, V. K. (1994). On the Variation of Cloud Condensation Nuclei in Association with Cloud Systems at a Mountain-Top Location, *Atmos. Res.*, 31:13-39.

Fukuta, N. and Saxena, V. K. (1979a). A Horizontal Thermal Gradient Cloud Condensation Nucleus Spectrometer, *J. Appl. Meteor.*, 18:1352-1362.

Fukuta, N. and Saxena, V. K. (1979b). The Principle of a New Horizontal Thermal Gradient Cloud Condensation Nucleus Spectrometer, *J. Rech. Atmos.*, 13:169-188.

Hudson, J. G. (1989). An Instantaneous CCN Spectrometer, *J. Atmos. Oceanic Technol.*, 6:1055-1065.

Li, Y. Q., Davidovits, P., Shi, Q., Jayne, J. T., Kolb, C. E., and Worsnop, D. R. (2001). Mass and Thermal Accommodation of H_2O(g) on Liquid Water as a Function of Temperature, *J. Phys. Chem. A.*, 105:10627-10634.

Nenes, A., Chuang, P. Y., Flagan, R. C., and Seinfeld, J. H. (2001a). A Theoretical Analysis of Cloud Condensation Nucleus (CCN) Instruments, *J. Geophys. Res.*, 106:3449-3474.

Nenes, A., Ghan, S., Abdul-Razzak, H., Chuang, P. Y., and Seinfeld, J. H. (2001b). Kinetic Limitations on Cloud Droplet Formation and Impact on Cloud Albedo, *Tellus Ser. B*, 53:133-149.

Pruppacher, H. R. and Klett, J. D. (1996) *Microphysics of Clouds and Precipitation*. Kluwer Academic Publishers, Dordrecht, The Netherlands.

Roberts, G. C. and Nenes, A. (2003). A Continuous-Flow Longitudinal Thermal-Gradient CCN Chamber for Airborne Measurements, manuscript in preparation.

Saxena, V. K. (1996). Bursts of Cloud Condensation Nuclei (CCN) by Dissipating Clouds at Palmer Station, Antarctica, *Geophys. Res. Lett.*, 23:69-72.

Saxena, V. K. and Carstens, J. C. (1971). On the Operation of Cylindrical Thermal Diffusion Cloud Chambers, *J. Rech. Atmos.*, 5:11-23.

Shaw, R. A., and Lamb, D. (1999). Experimental Determination of the Thermal Accommodation and Condensation Coefficients of Water, *J. Chem. Phys.*, 111:10659-10663.

Sinnarwala, A. M. and Alofs, D. J. (1973). A Cloud Nucleus Counter with Long Available Growth Time, *J. Appl. Meteorol.*, 12:831-835.

Snider, J. R. and Brenguier, J.-L. (2000). Cloud Condensation Nuclei and Cloud Droplet Measurements during ACE-2, *Tellus Ser. B,* 52:828-842.

Twomey, S. (1963). Measurements of Natural Cloud Nuclei, *J. Rech. Atmos.*, 1:101-105.

VanReken, T. M. (2004). Understanding the Relationship between Aerosols and Clouds: Field Investigations and Instrument Development, Ph. D. thesis, California Institute of Technology, Pasadena, California.

VanReken, T. M., Rissman, T. A., Roberts, G. C., Varutbangkul, V., Jonsson, H. H., Flagan, R. C., and Seinfeld, J. H. (2003). Towards Aerosol/CCN Closure during CRYSTAL-FACE, *J. Geophys. Res., 108*(D20), 4633, doi:10.1029/2003JD003582, 2003.

Table 1. Operating conditions and parameters for the original FSCS Design (Fukuta and Saxena, 1979a) and the Baseline Design.

Parameter	Original FSCS	Baseline
Length of chamber from inlet to exit, m	0.838	0.838
Width (*W*) of chamber, m	0.191	0.070
Height (*H*) of chamber, m	0.018	0.018
Distance at which walls become saturated, m	0.168	0.168
Inlet Pressure, Pa	1.013×10^5	1.013×10^5
Inlet Relative Humidity, %	100	100
Inlet Temperature, K	283	283
Hot Tip Temperature, K	288	288
Cold Tip Temperature, K	283	283
Volumetric Flow Rate, $m^3\ s^{-1}$	8.5×10^{-5}	3.5×10^{-5}
Design Criterion, *B*	4.48	0.70

Figure Captions

Figure 1. Schematics of cross sections for (a) the rectangular geometry of the original FSCS and the Baseline design; and (b) the proposed trapezoidal geometry. In both cases, heat travels from T_{H0} to T_{C0} through the conductive material along the coordinate s.

Figure 2. Equilibrium velocity profiles near the high supersaturation end of the growth chamber for the original FSCS configuration and this study's Baseline configuration. The FSCS profile is taken at z =0.015 m, and the Baseline profile is from z =0.010 m. The centerline of each chamber is located at y = 0.000 m, and dotted lines represent the hot and cold plates. Negative velocities in the original FSCS profile indicate flow reversal occurs for the conditions simulated.

Figure 3. Simulation results for the original FSCS design (Figure 1a). (a) Centerline supersaturation profiles for several values of z; and (b) particle growth curves for those streamlines. These results are for an ammonium sulfate aerosol with an assumed accommodation coefficient of 1.0.

Figure 4. As in Figure 3, but for the Baseline instrument design.

Figure 5. The variation in the centerline velocity for several trapezoidal geometries. ΔH = 0.000 m for the Baseline design. The velocity values are taken at a point where the equilibrium flow field is established.

Figure 6. Particle growth curves for several values of ΔH. Only the upper and lower boundaries of the resolvable supersaturation range are presented.

Figure 7. Centerline supersaturation profiles for the case where ΔH = 0.010 m. Note the distances required to reach the equilibrium supersaturation on different streamlines, compared with Figure 4b.

Figure 8. Particle growth curves for several values of ΔT. To prevent overlap, the growth curves for z = 0.010 m and z = 0.050 m are offset. The values for these curves are found on the right axis.

Figure 9. Particle growth curves for several values of Q. The upper and lower boundaries to the resolvable supersaturation range are presented.

Figure 10. As in Figure 3, for an optimized instrument configuration.

Figure 11. Particle growth curves indicating the dependence of the instrument performance on (a) particle composition and (b) the mass accommodation coefficient. The curves in (b) result when the sample aerosol is pure ammonium sulfate with the accommodation coefficient set to 0.04. The additional curve in (a) is to indicate the difference in the results of the two aerosol growth models (see text).

Figure 1a

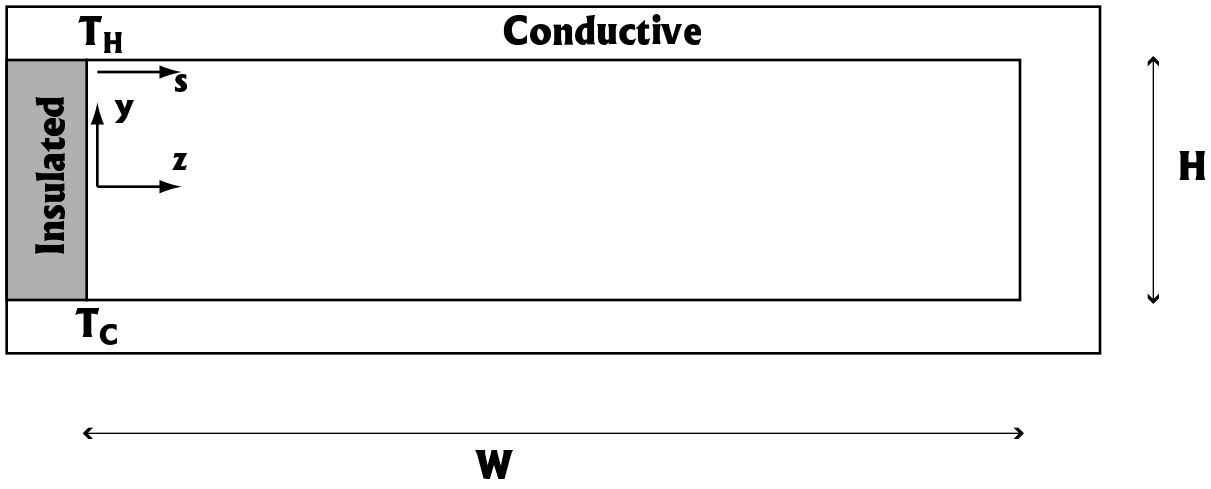

Figure 1b

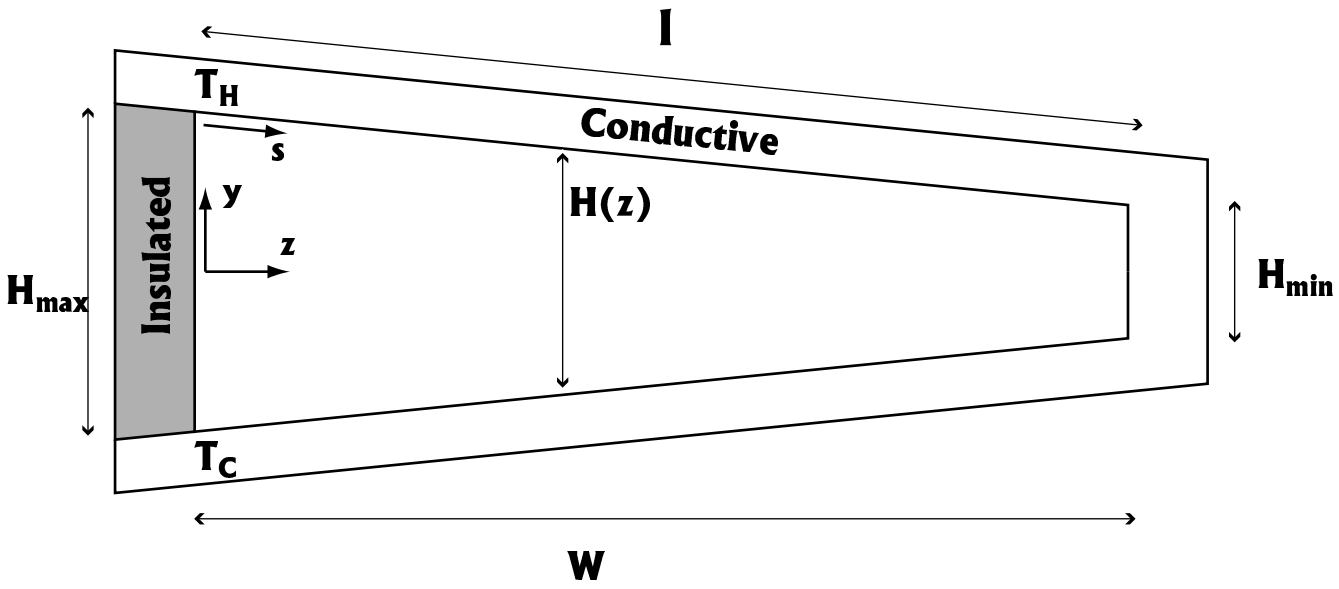

Figure 2

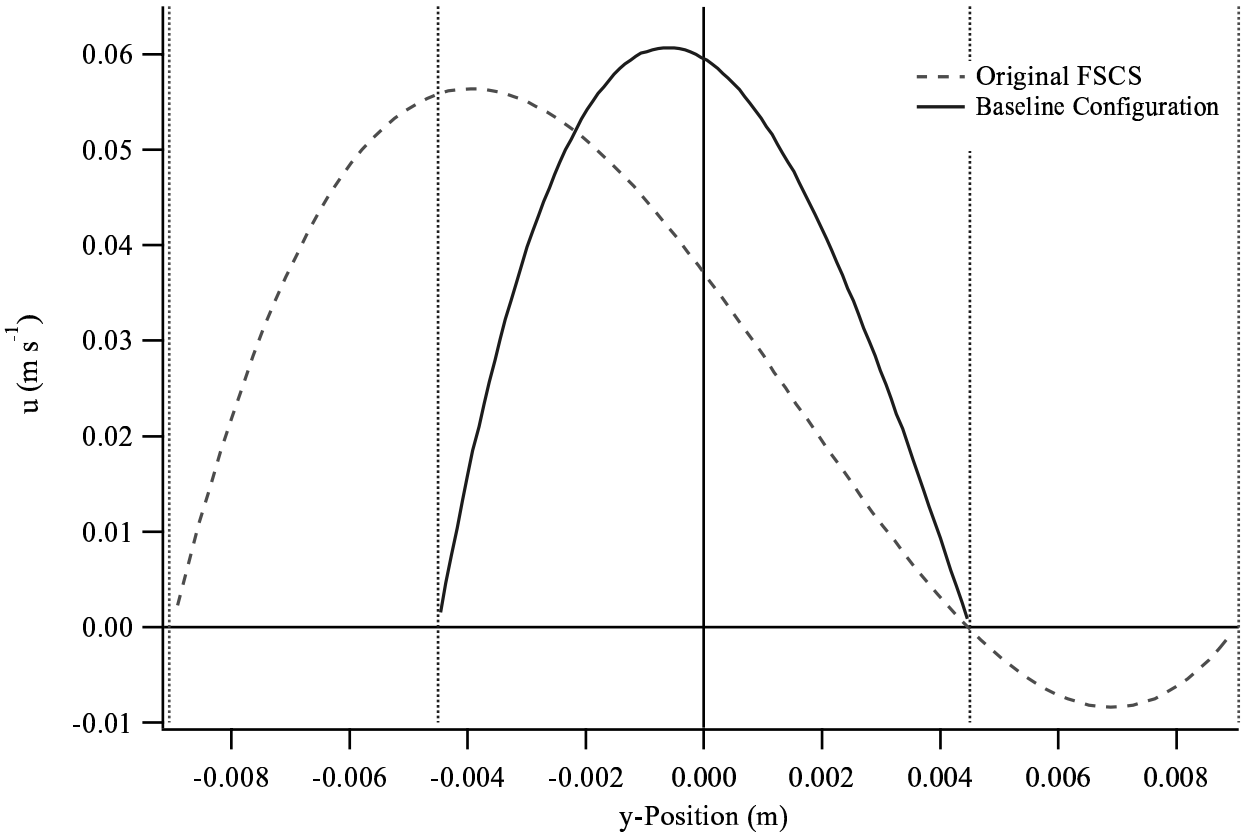
0.06
0.05
0.04
0.03
0.02
0.01
0.00
-0.01
u (m s-1)
-0.008
-0.006
-0.004
-0.002
0.000
0.002
0.004
0.006
0.008
y-Position (m)
Original FSCS
Baseline Configuration

Figure 3a

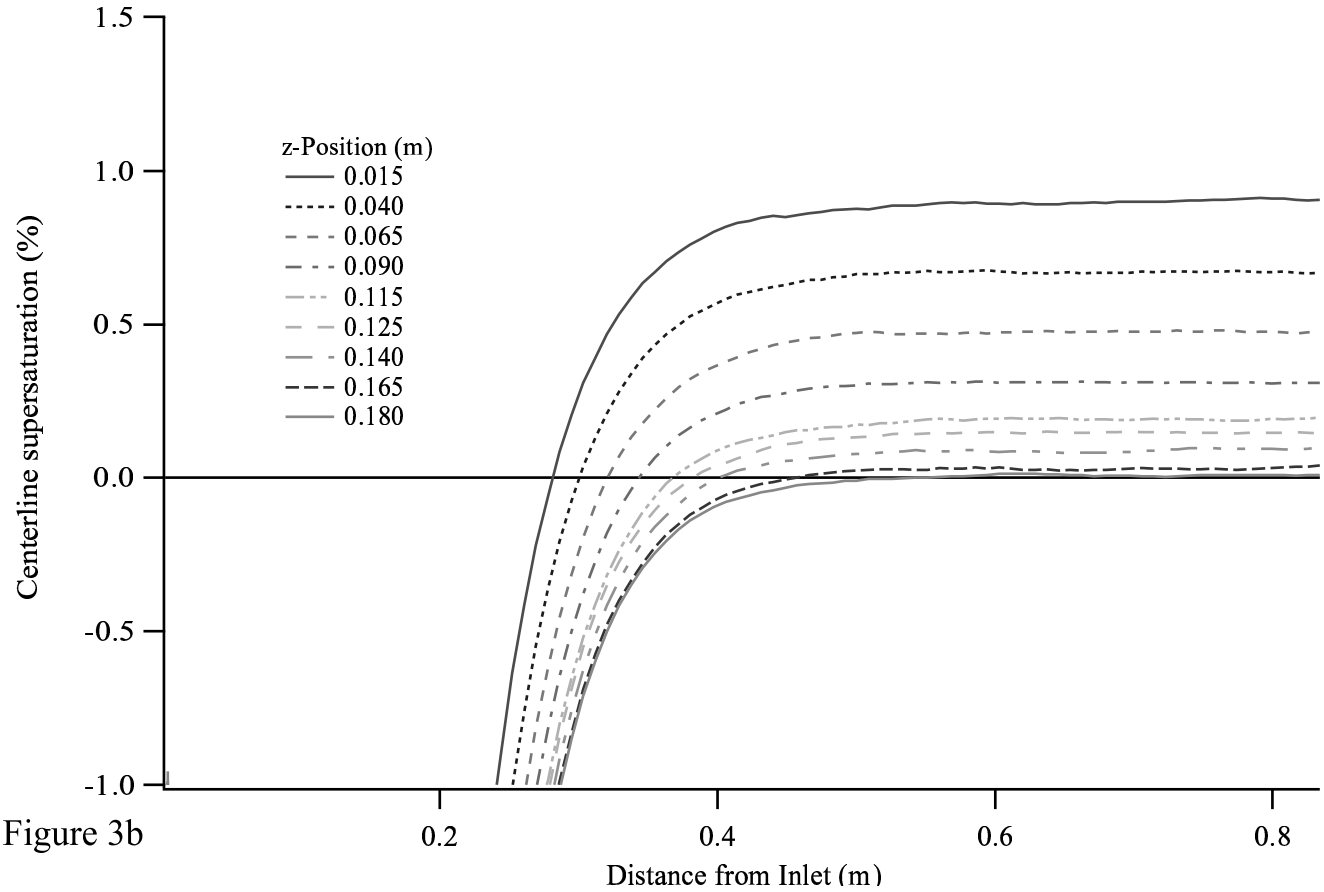

Figure 3b

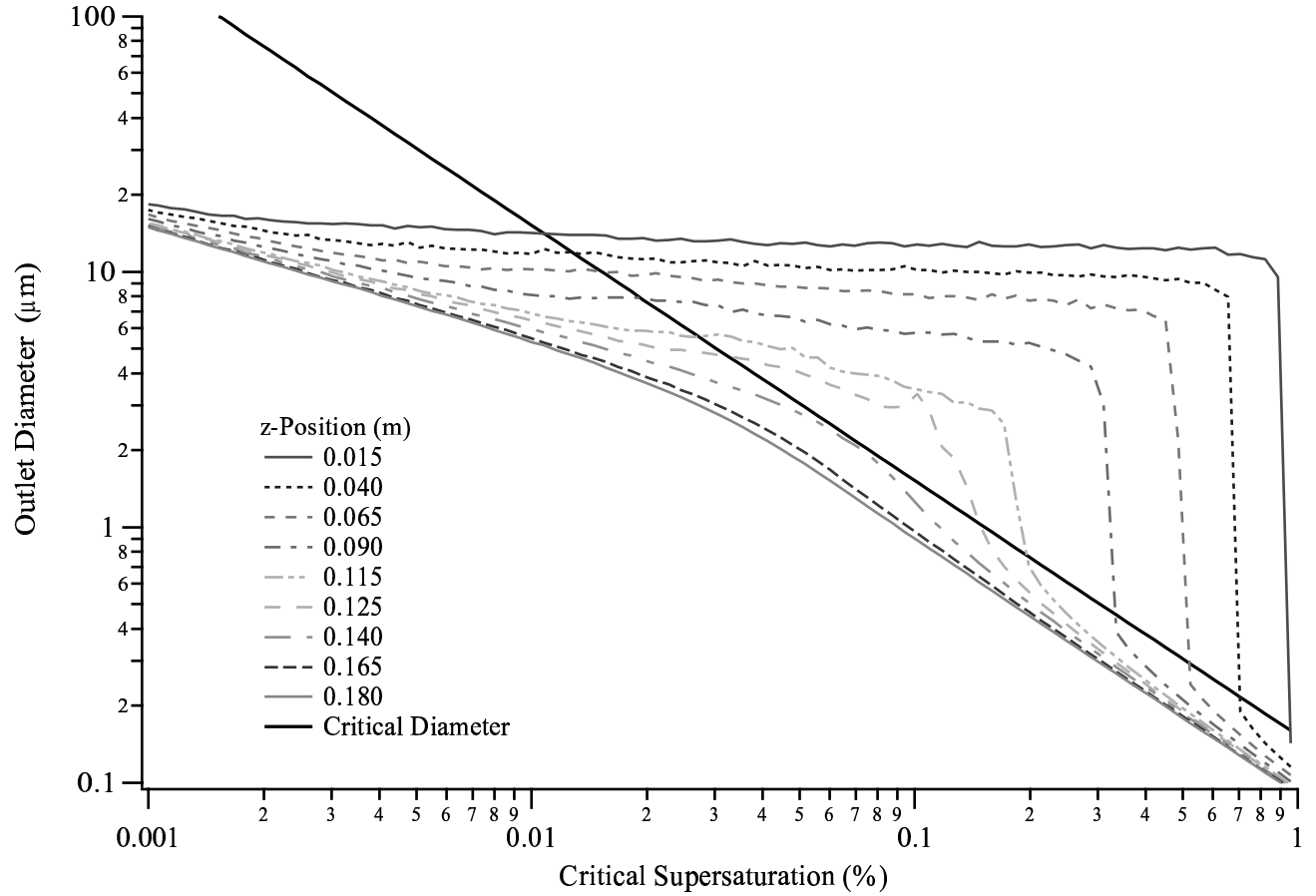

Figure 4a

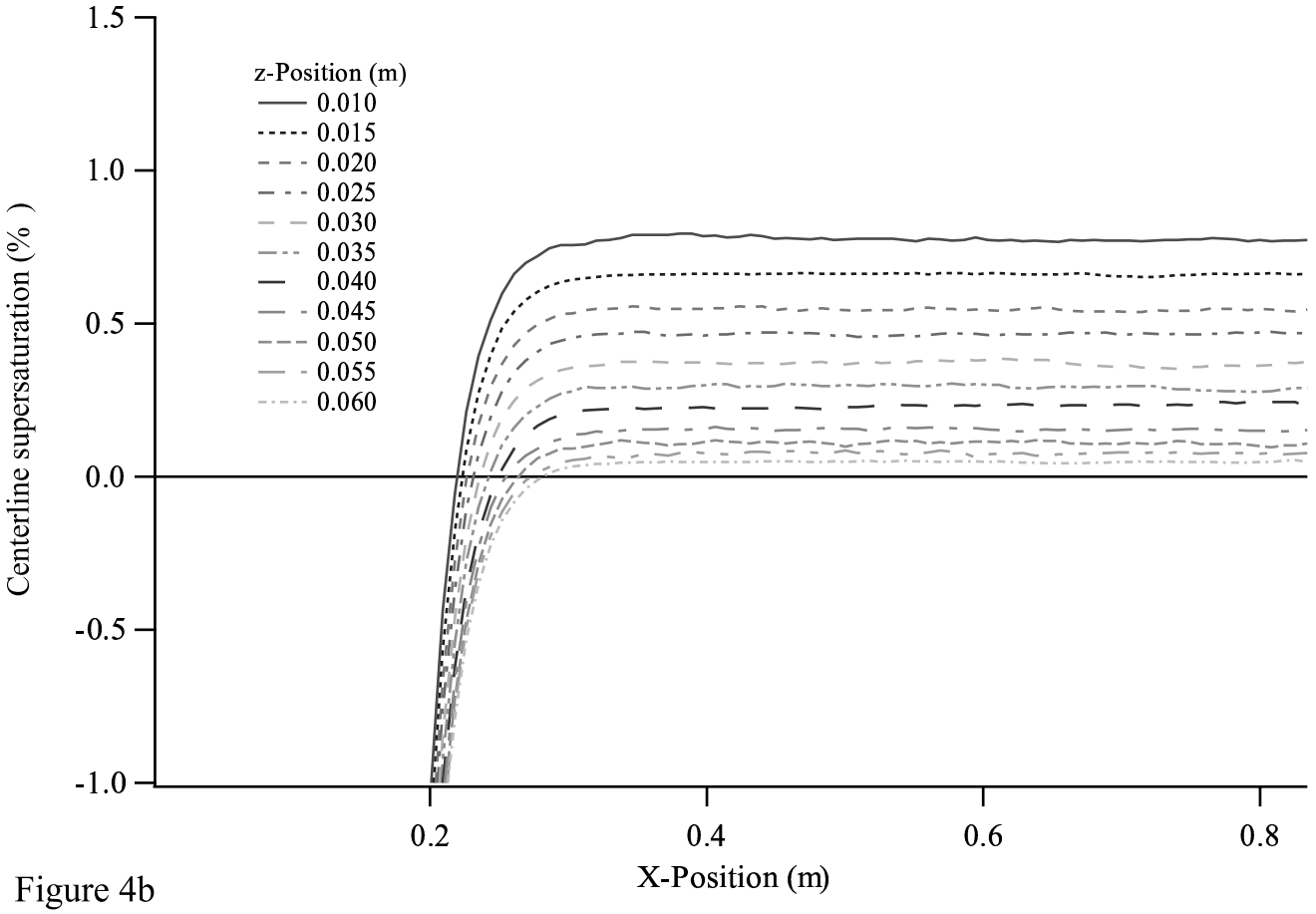

Figure 4b

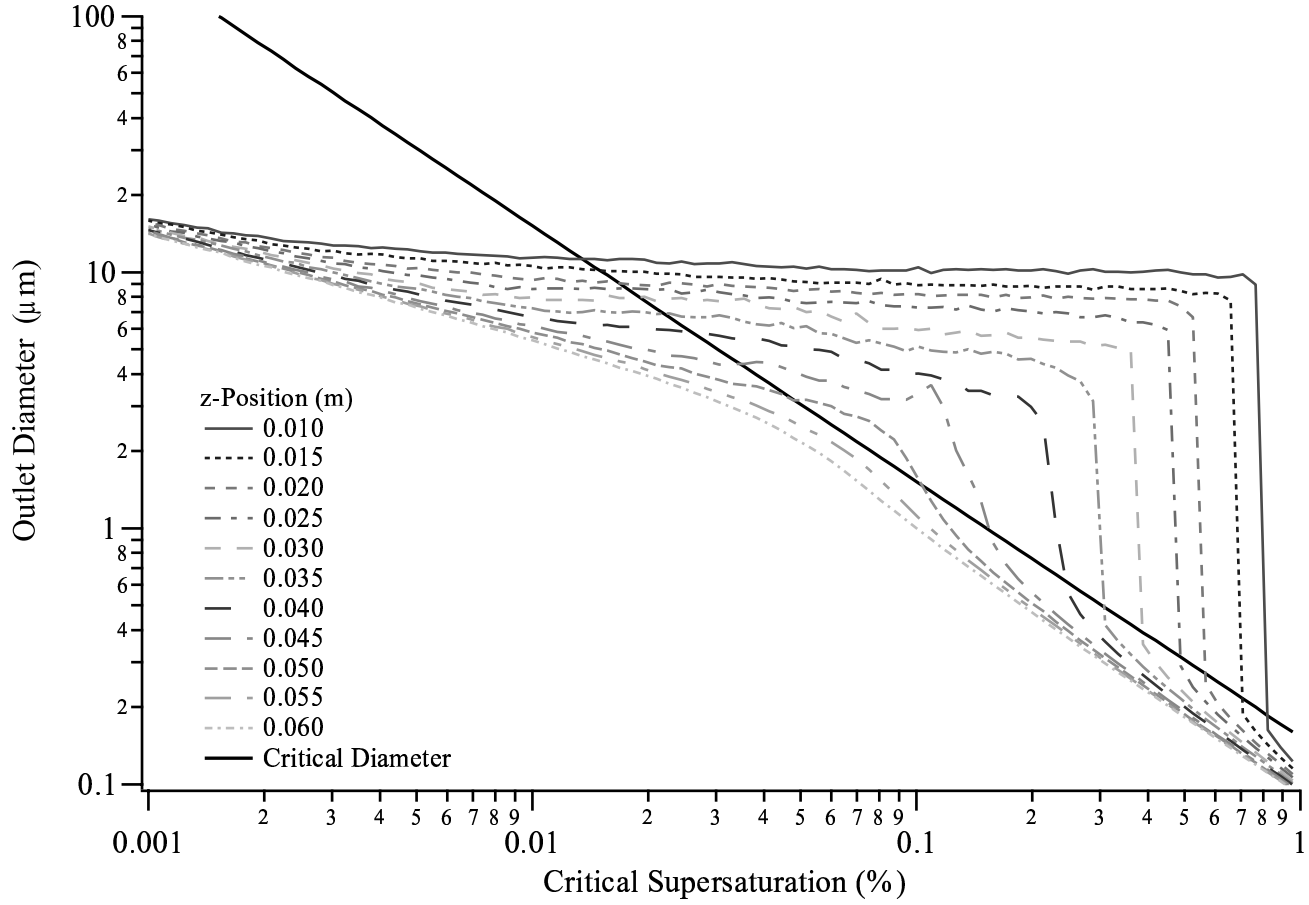

Figure 5

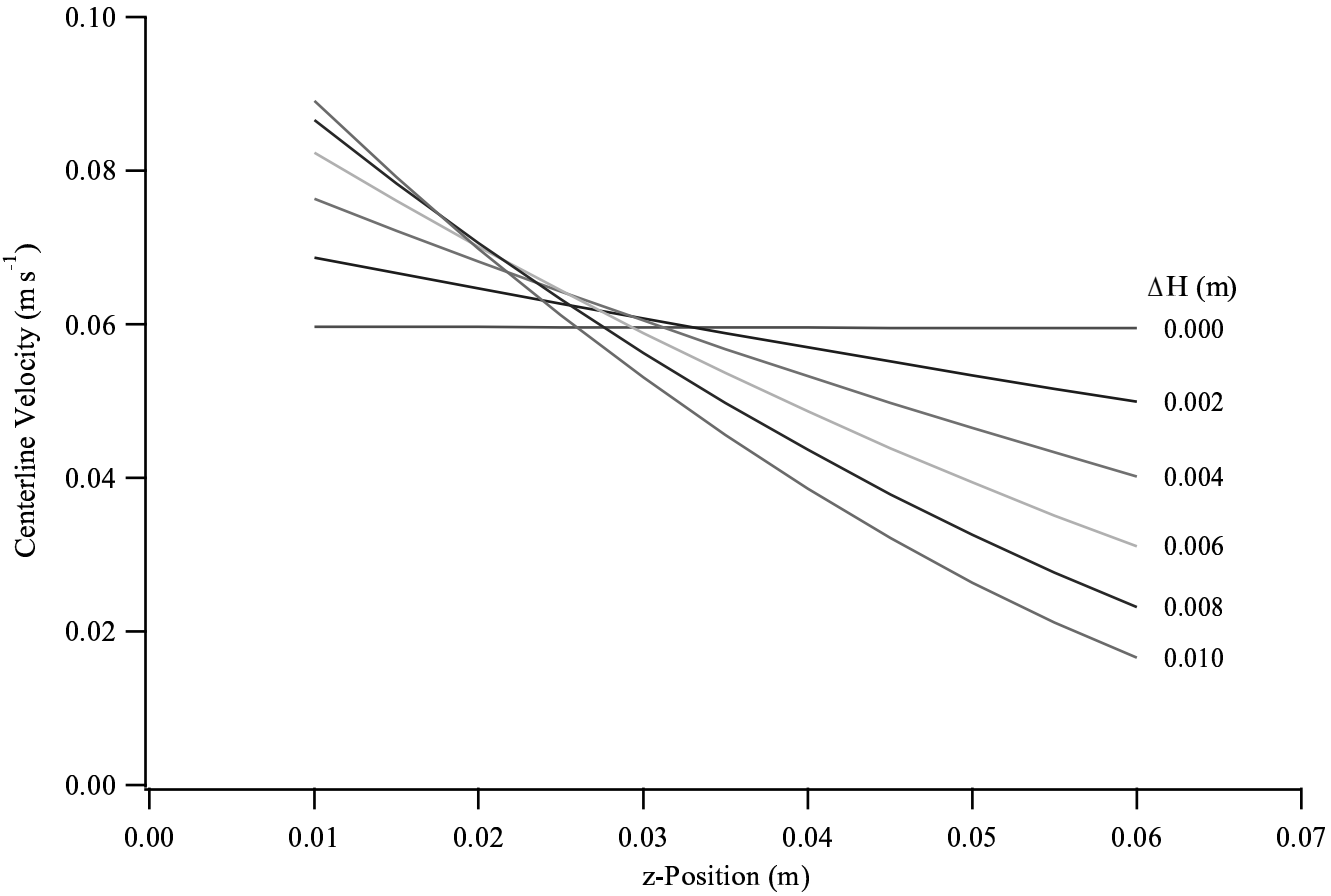
0.10
0.08
0.06
0.04
0.02
0.00
Centerline Velocity (m s-1)
0.00
0.01
0.02
0.03
0.04
0.05
0.06
0.07
z-Position (m)
ΔH (m)
0.000
0.002
0.004
0.006
0.008
0.010

Figure 6

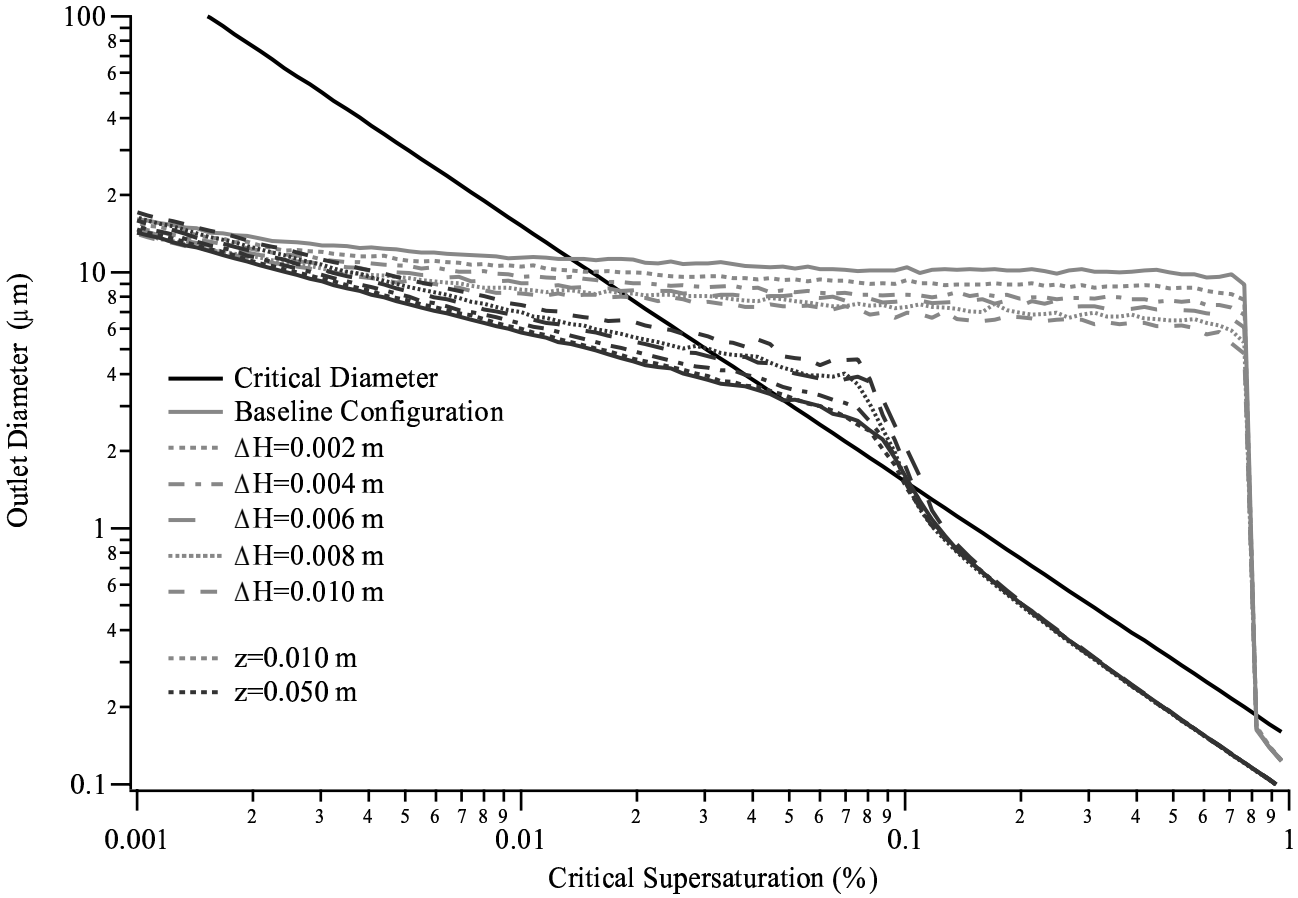
Outlet Diameter (μm)
Critical Supersaturation (%)
Critical Diameter
Baseline Configuration
ΔH=0.002 m
ΔH=0.004 m
ΔH=0.006 m
ΔH=0.008 m
ΔH=0.010 m
z=0.010 m
z=0.050 m
100
10
1
0.1
0.001
0.01
0.1
1

Figure 7

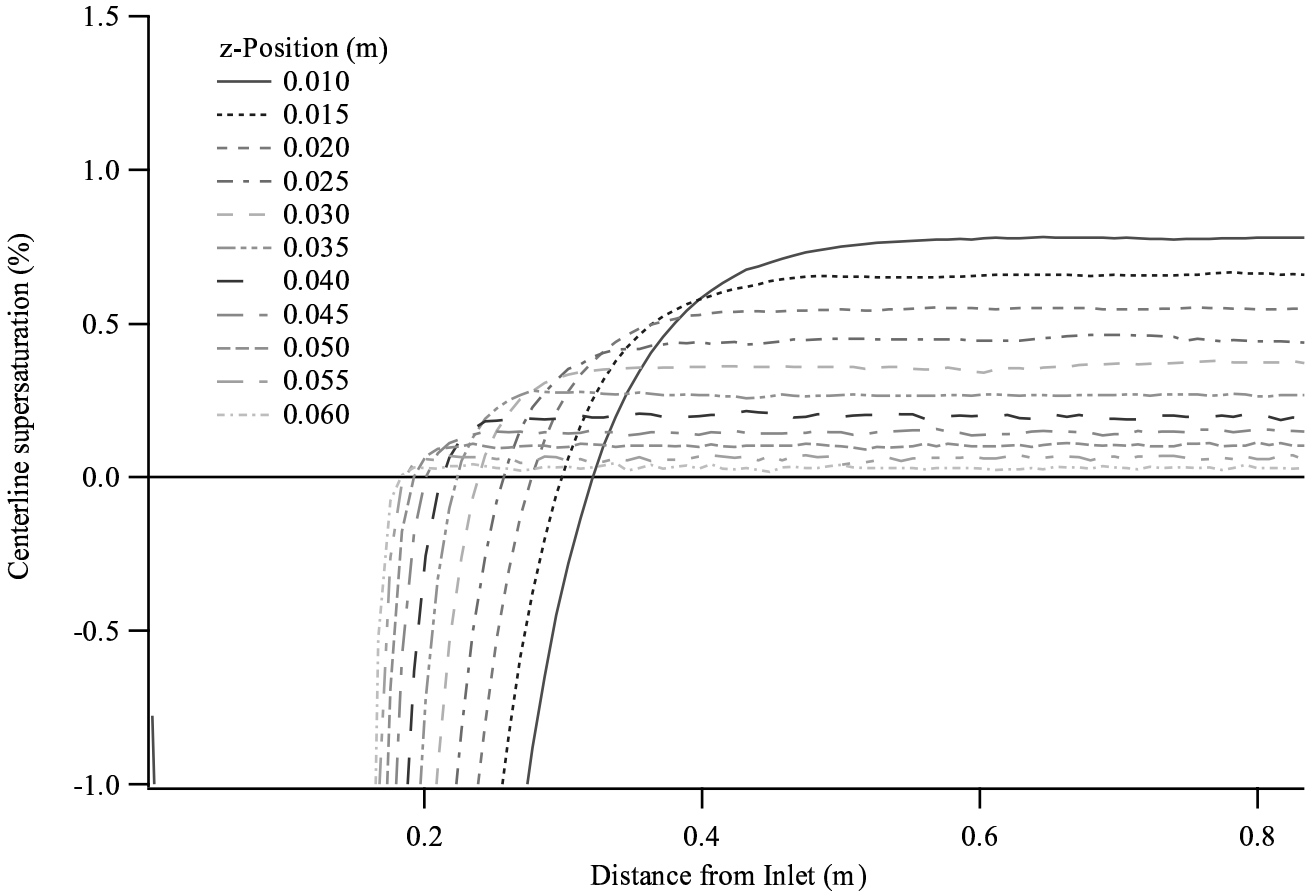
z-Position (m)
0.010
0.015
0.020
0.025
0.030
0.035
0.040
0.045
0.050
0.055
0.060
Centerline supersaturation (%)
1.5
1.0
0.5
0.0
-0.5
-1.0
0.2
0.4
0.6
0.8
Distance from Inlet (m)

Figure 8

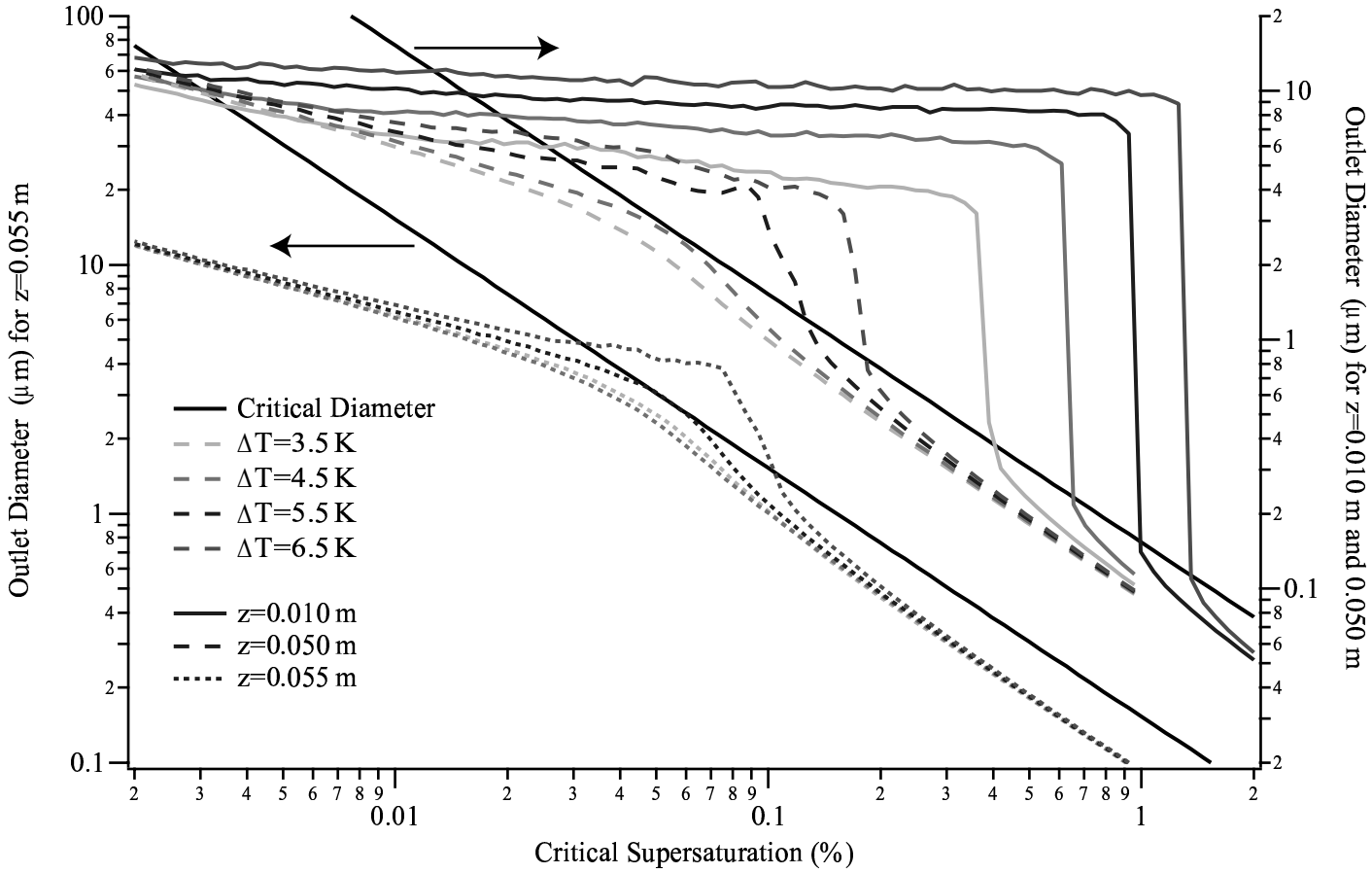
Outlet Diameter (μm) for z=0.055 m
Outlet Diameter (μm) for z=0.010 m and 0.050 m
Critical Supersaturation (%)
Critical Diameter
ΔT=3.5 K
ΔT=4.5 K
ΔT=5.5 K
ΔT=6.5 K
z=0.010 m
z=0.050 m
z=0.055 m

Figure 9

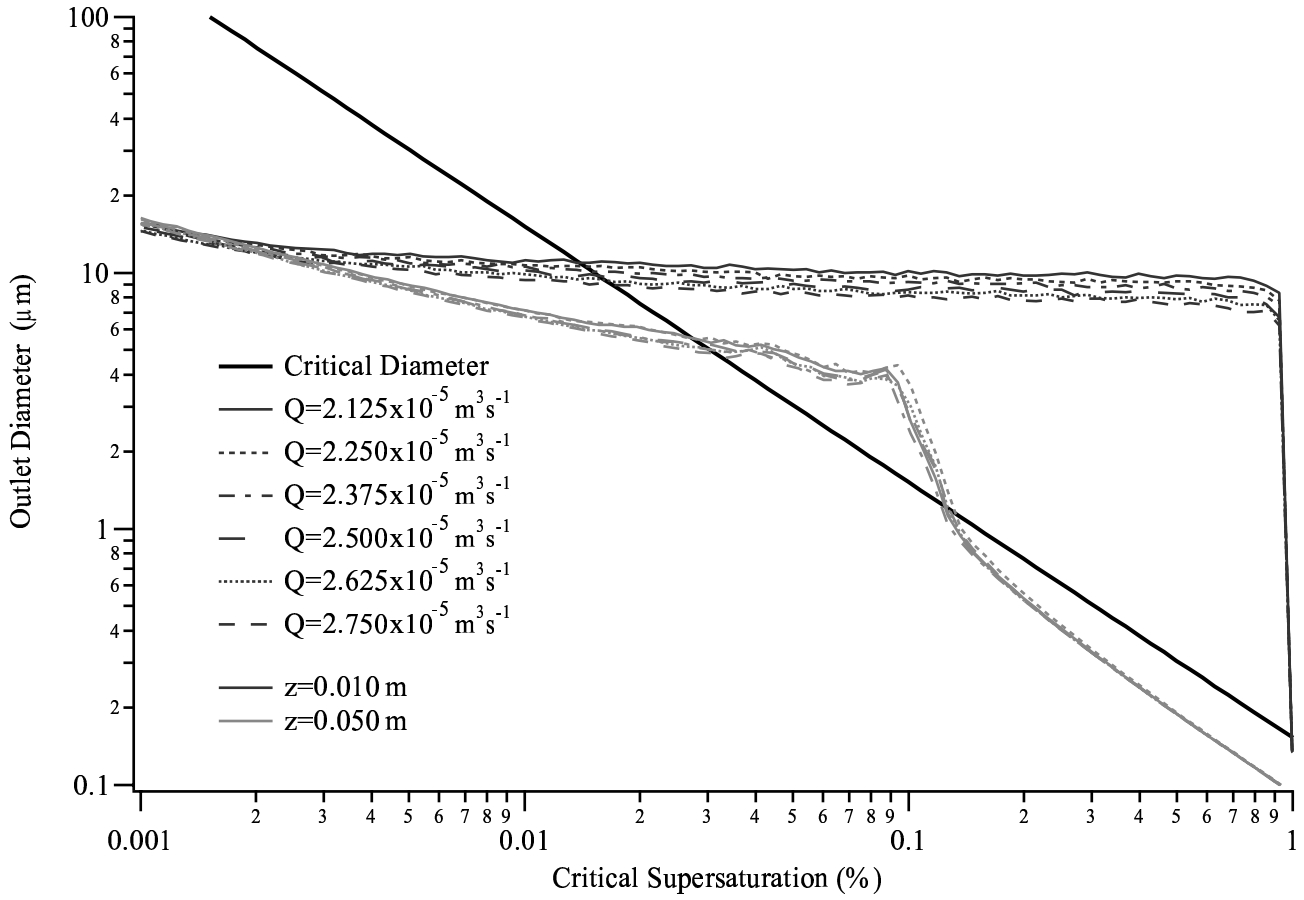
Outlet Diameter (μm)
Critical Supersaturation (%)
Critical Diameter
Q=2.125x10^-5 m^3s^-1
Q=2.250x10^-5 m^3s^-1
Q=2.375x10^-5 m^3s^-1
Q=2.500x10^-5 m^3s^-1
Q=2.625x10^-5 m^3s^-1
Q=2.750x10^-5 m^3s^-1
z=0.010 m
z=0.050 m
100
10
1
0.1
0.001
0.01
0.1
1

Figure 10a

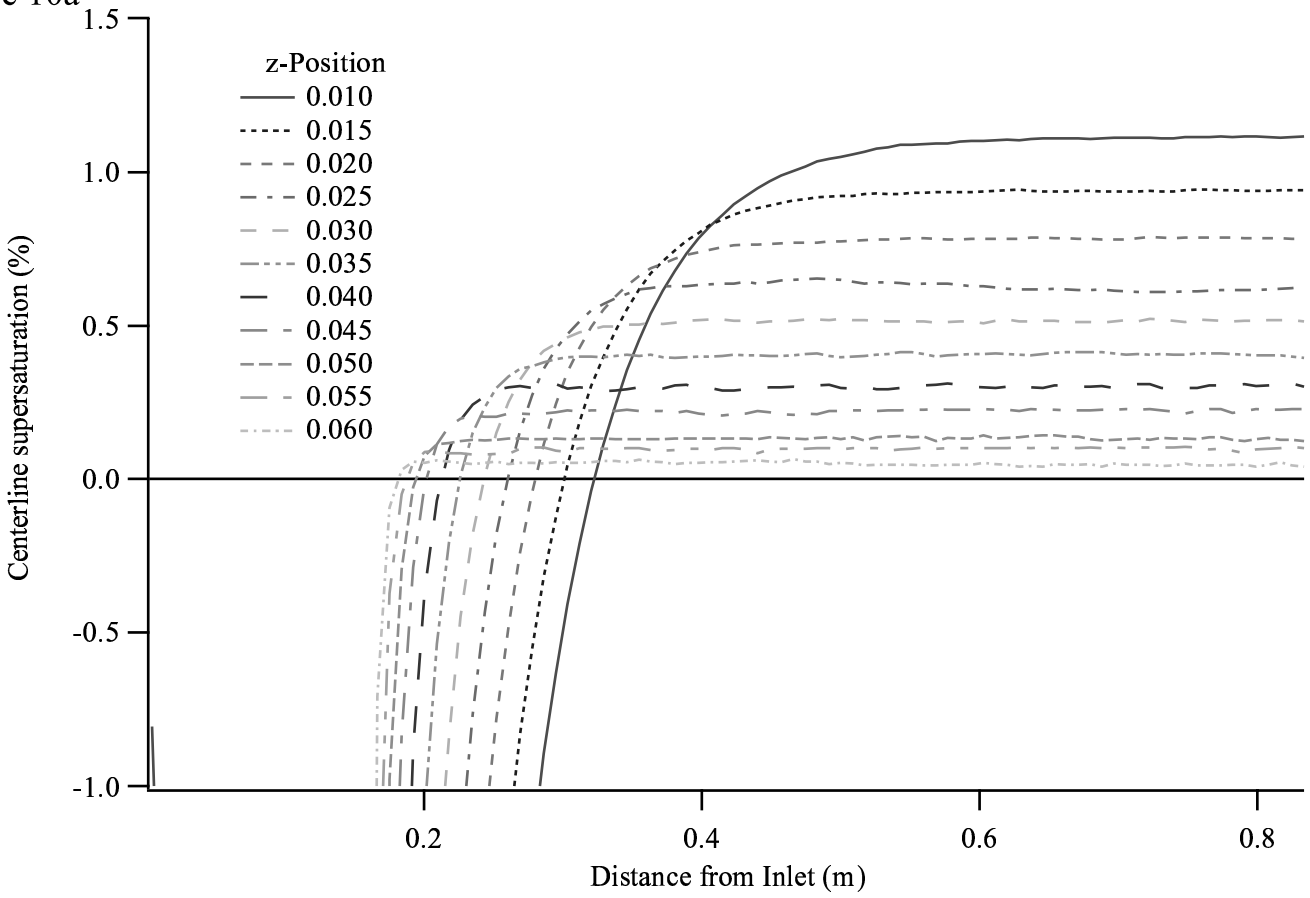

Figure 10b

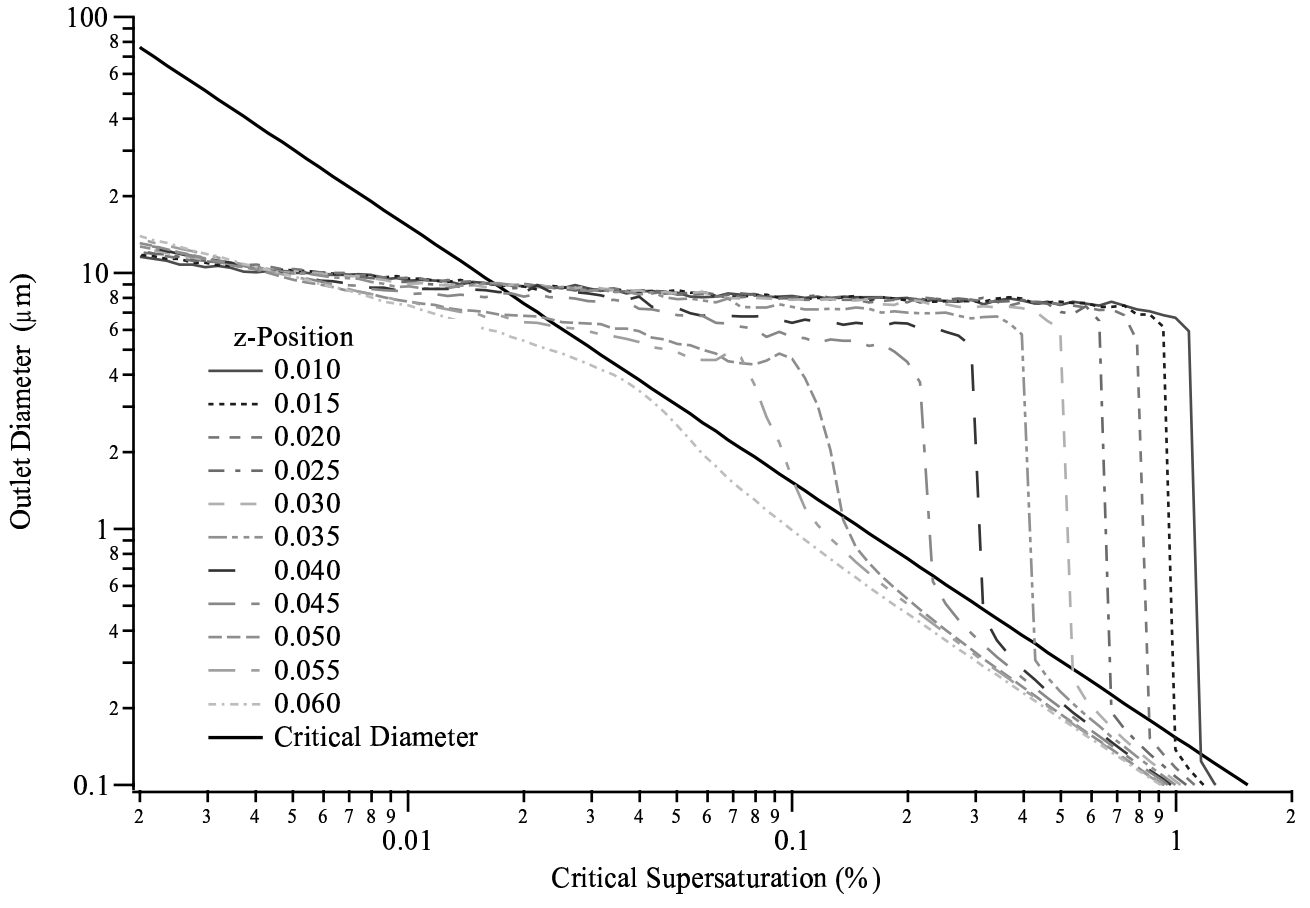

Figure 11a

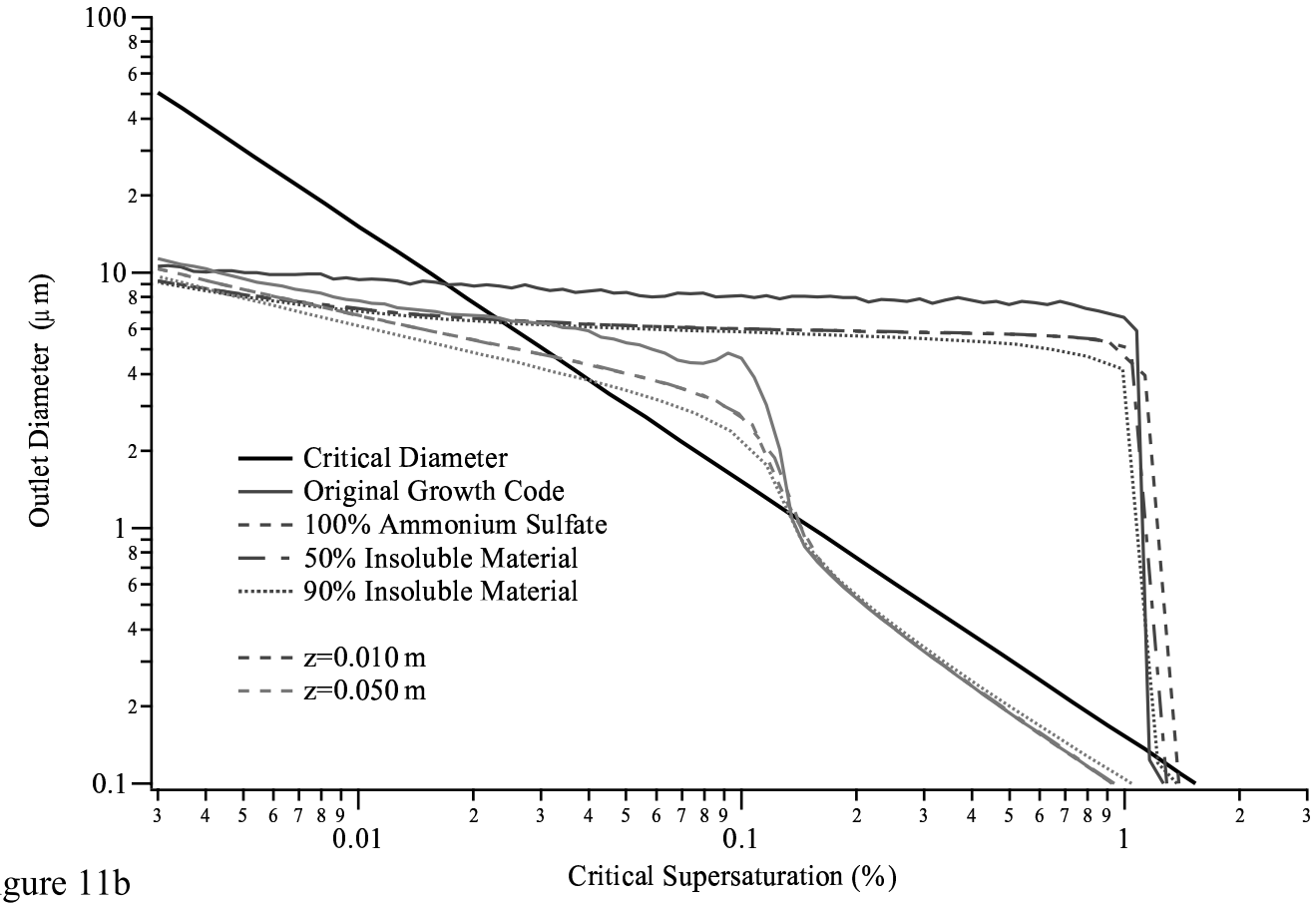

Figure 11b